Magnetization Dynamics of Superparamagnetic Nanoparticles for Magnetic Particle Spectroscopy and Imaging

Magnetization dynamics theory of superparamagnetic nanoparticles for Magnetic Particle Spectroscopy and Imaging

Gabriele Barrera,* Paolo Allia, and Paola Tiberto
INRiM, Advanced Materials Metrology and Life Sciences, Torino, I-10135, Italy
(Dated: April 27, 2022)

An exact theory is developed with the aim of assessing the properties of the harmonics spectrum of the dynamic magnetization originating from superparamagnetic nanoparticles submitted to a high-frequency driving field. The magnetization is assumed to be always close to equilibrium at the frequencies of interest, so that it can be still described by the anhysteretic Langevin function. The theory, valid for an extended range of values of physical properties and sizes of particles, is aimed at interpreting typical results of Magnetic Particle Spectroscopy and Imaging. The analytical framework is exploited to get a deeper knowledge of the spectral properties of nanoparticle magnetization and to assess the persistence of the superparamagnetic behaviour at the operating frequencies. The spectral properties of the time-dependent Langevin function are analyzed in detail and compared with experimental results on polydisperse, immobilized nanoparticles. The system function usually exploited in Magnetic Particle Imaging is calculated with precision as a function of both particle size and driving field's amplitude.

I. INTRODUCTION

In recent years, fundamental and application-oriented research on magnetic nanoparticles has been increasingly addressed to high-frequency properties [1–7]. The interest is boosted by a great number of novel applications where nanoparticles (mostly composed of iron oxides [8]) may act as tracers [9, 10], pointlike heat sources [11–14], encoding elements [15], microwave devices[16] and are activated, stimulated or interrogated by a high-frequency driving field. In a remarkable fraction of practical applications, the nanoparticles are not suspended in a fluid nor freely displacing/rotating in space, but they are - through choice or happenstance - immobilized in some medium in such a way that their magnetic response is determined by the Néel's relaxation mechanism only [17, 18].

Present and prospective high-frequency applications of magnetic nanoparticles range from biomedicine to energy saving and data encryption, and include advanced diagnostic tools such as Magnetic Particle Spectroscopy (MPS) [19–22] and Magnetic Particle Imaging (MPI) [23–27], specific therapies for precision nanomedicine such as Magnetic Hyperthermia [12, 28, 29], communicating objects for miniaturized product security and the Internet of Nano Things [15, 30], advanced devices for the Information and Communication Technology [6]. Application areas where the particles' response to a high-frequency magnetic field is the key factor have rapidly paralleled or even surpassed the ones where particles are in static or quasi-static conditions.

Although a detailed knowledge of the magnetic properties of nanoparticles is mandatory to fully exploit the great potentialities of this class of nanomaterials, the fundamentals of their high-frequency magnetism have not been investigated so far to the same depth of static or quasi-static properties, for which a shared viewpoint supported by an extensive literature exists [31–33].

In most of the present-day high frequency applications of magnetic nanoparticles, the individually responding elementary units are typically considered to be superparamagnetic, with magnetization described by the Langevin function [25, 34]. For immobilized particles, this means that Néel's relaxation time has to be shorter than one driving field's period; when this condition is satisfied, the distribution of magnetic moments in space by effect of a time-dependent magnetic field can be assumed to retain the same functional form as under a constant field. [35] Indeed, a number of particles synthesized in laboratories or industrially produced and typically made of magnetite have structure, morphology and intrinsic magnetic properties which allow the Langevin-function approach to be adopted. In particular, the energy barrier between equilibrium directions of the magnetization vector is tailored to be sufficiently low to guarantee a bona fide room-temperature superparamagnetic behaviour of the magnetic units non only in static conditions but also at moderate to high magnetizing frequencies [36, 37].

In this case, the cyclic magnetization process is pictured as virtually unaffected by magnetic hysteresis. Such a simplified picture is largely acceptable in many applications, particularly when the particles operating in the 1 - 25 kHz frequency range act as tracers [20, 25]; however, this is no longer true in applications at higher frequency (in the 50 - 200 kHz range) where the main advantage of using magnetic nanoparticles mostly resides in their ability to release energy as heat, such as in Magnetic Hypertermia; in the latter case, the existence of wide magnetic hysteresis loops is a key factor for producing the desired effect [28, 38].

In high-frequency applications of nanoparticles for diagnostics and decoding a central role is played by the harmonics of the frequency spectrum of the magnetization produced by the driving field. The richness of the magnetization spectrum basically results from

* Second.Author@institution.edu

the intrinsic nonlinearity of the Langevin function with respect to its argument [39]: higher-order harmonics of the frequency spectrum emerge in a quite natural way from the powers of the argument which appear in any suitable series representation of the Langevin function. The same feature is observed by directly simulating the magnetization waveform through the time-dependent Langevin function, subsequently evaluating the harmonics of the simulated magnetization signal [37, 40]. Although the link between nonlinearity of the Langevin function and presence of higher-order spectral harmonics is usually taken for granted [25, 34, 39] a complete analytic treatment of the nonlinear problem is still lacking. In some cases, the amplitudes of the first few harmonics were approximately calculated starting from a representation of the Langevin function which is however not always useful [41, 42]. In other approaches, the relationship between magnetization and driving field was assumed to be strictly linear, and the nonlinearity of the Langevin function was approximately taken into account by an ad hoc modification of the magnetic susceptibility [43–45]. However, in most applications the amplitude of the driving field is often such that an approach based on the linear response theory is hardly applicable.

In this paper we show that the spectrum of harmonics of the time-dependent Langevin function can be exactly known in full through an analytical treatment which does not require any simplifying assumptions. In this way, the features of the time-dependent Langevin function are assessed in a comprehensive way and the properties of the spectral harmonics are presented in detail. The results of the calculations allow one to predict the behaviour of the spectral harmonics as functions of operating parameters such as the driving field's amplitude and of physical properties such as nanoparticle size and saturation magnetization or temperature of operation. Such an outcome is of central interest for MPS.

In addition, the theory makes it possible to give an exact expression of the third harmonic of the magnetization as a function of the value of a constant bias field superimposed to the high-frequency driving field, solving the problem of determining with high precision the system function (SF), which plays a central role in MPI [45–47].

Spectroscopy and imaging based on magnetic nanoparticles have multiple points of contact and can therefore be the subject of a common theoretical treatment. It should be remarked that MPS can be exploited both to characterize magnetic tracers for MPI applications [40] and to make quantitative the MPI signals [48].

A qualifying point of the proposed analytical treatment is the quantitative comparison between the predictions of an exact theory and the results of real measurements conducted on samples made of immobilized nanoparticles. This is done in a specific Section using experimental data partly taken from the literature and partly specifically realized for this work. The excellent agreement between theory and experimental results permits to extract an accurate information about the distribution of particle sizes in all examined samples.

Advancing in the knowledge of superparamagnetic particles at high frequency allows a better grasp of the physical aspects underlying experimental results and technical applications in magnetic-particle spectroscopy and imaging. Although modelling of magnetic dynamics for magnetic nanoparticles may require in-depth theories [49] or simulations [50] in cases when intra- and interparticle properties such as effective anisotropy and dipolar interaction cannot be disregarded, the time-dependent Langevin-function treatment has the great advantage of simplicity in the description of dynamic magnetization, which makes the analytical problem of finding the spectral harmonics exactly solvable.

II. MATHEMATICAL TOOLS

We consider a set of monodisperse, spherical nanoparticles of size D and volume $V = \frac{\pi}{6}D^3$ having spontaneous magnetization M_s. In thermal equilibrium conditions at the temperature T (higher than the blocking temperature) [33] the magnetization of the system submitted to a magnetic field H is usually expressed by the Langevin function of argument y:

$$L(y) = \coth(y) - \frac{1}{y} \tag{1}$$

where $y = M_s V H/k_B T$. When the magnetic field is a harmonic function of time of frequency f and angular frequency $\omega = 2\pi f$ such as:

$$H(t) = H_0 + H_V \cos(\omega t), \tag{2}$$

the magnetization $M(t) = M_s L[(\omega t)]$ contains in principle an infinite number of odd harmonics [25]. In Equation 2, the constant H_0 is the bias field, determined in each point of the scanned region by the presence of a magnetic field gradient, a typical feature of MPI [25, 34]. The bias field can be zero or take positive values, and H_V is the vertex field, i.e., the maximum amplitude of the oscillating component; typically, H_0 is zero in applications such as MPS.

Aim of the work is to derive an exact, analytical expression of the amplitude of the harmonics. As a matter of fact, Equation 1 is not a suitable starting point when one looks for the Fourier expansion of the magnetization signal. Three specific series developments of the Langevin function will be used in this paper.

1. The usual Taylor series development of the Langevin function:

$$L(y) = \sum_{k=1}^{\infty} \frac{2^{2k}}{(2k)!} B_{2k}\, y^{2k-1} \approx \approx \frac{1}{3}y - \frac{1}{45}y^3 + \frac{2}{945}y^5 - ... \quad (3)$$

(where the B_{2k}'s coefficients are the even Bernouilli's numbers) [51] works around $y = 0$ but has the disadvantage of being valid only when $|y| < \pi$ [51]. This means that the Taylor series development of $L(\omega t)$ cannot be used when $[\gamma(H_0 + H_V)] \geq \pi$. For instance, considering magnetite particles with $D = 15$ nm and $M_s = 300$ emu/cm^3 at room temperature, the maximum vertex field at zero bias ($H_0 = 0$) which permits to use Equation 3 is about 245 Oe only. Using a higher vertex field ($H_V = 400$ Oe), the maximum particle size must not exceed 13 nm in order to use this development. The examples clearly show that the range of validity of Equation 3 is somewhat limited.

2. An equivalent, if less common development of the Langevin function (valid for any value of y between 0 and ∞) is [51]:

$$L(y) = \frac{2y}{\pi^2} \sum_{k=1}^{\infty} \frac{1}{(y/\pi)^2 + k^2} \equiv 2y \sum_{k=1}^{\infty} \frac{1}{y^2 + k^2\pi^2} \quad (4)$$

3. Finally, for large values of y (specifically: when the magnetic field is always well above zero for any pair of values of H_0 and H_V) the following expression of $L(y)$ can be used [51]:

$$L(y) = 1 - \frac{1}{y} + 2\sum_{n=1}^{\infty} e^{-2ny} \quad (5)$$

All the above expressions of the Langevin function will be exploited here. In particular:

- for $H_0 = 0$ as in the MPS practice, Equation 4 will be taken as the starting point of calculations, resulting in a general expression of all spectral harmonics valid for all parameter values;

- for $H_0 \neq 0$, as in the typical operating conditions of MPI, the treatment of Equation 4 poses great analytical difficulties, so that one has to resort to Equations 3 and 5, whose separate ranges of validity will be shown to overlap over an extended range of H_0 values.

The next Section is devoted to the development of an analytic expression of all odd harmonics of the magnetization signal in MPS conditions (i.e., at zero bias field), whilst Section *Analytic expression of the system function in MPI* contains a study of the third harmonic of the magnetization signal as a function of the bias field H_0 at constant H_V, i.e., in the typical operating conditions of MPI. In this way, an accurate representation of the system function is obtained.

As a final remark, the following calculations will give the analytical expressions of the amplitudes of the odd harmonics of $M(t)$. In typical applications such as MPS and MPI it is the induced voltage $V(t) \propto -dM/dt$ which is detected [41]. The absolute value of the harmonics of $V(t)$ is proportional (by a factor depending on the details of the pickup setup) to the product of the absolute value of the amplitude of the n-th harmonic of $M(t)$ multiplied by n.

III. ODD HARMONICS OF MAGNETIZATION AT ZERO BIAS FIELD

A. General Framework

Our starting point is Equation 4 where $y = \beta\cos(\omega t)$, with $\beta = M_s V H_v/k_B T$. Calling $x = \omega t$, one has:

$$L(x) = 2\sum_{k=1}^{\infty} \frac{\beta\cos x}{\beta^2\cos^2 x + k^2\pi^2} = 2\sum_{k=1}^{\infty} f_k(x) \quad (6)$$

Each term f_k is an even periodic function of x and can be developed as a Fourier series containing cosine terms only:

$$f_k(x) = \frac{a_{0k}}{2} + \sum_{n=1}^{\infty} a_{nk}\cos(nx) \quad (7)$$

where the a_{nk} coefficients are given by:

$$a_{nk} = \frac{1}{\pi}\int_{-\pi}^{\pi} \frac{\beta\cos x}{\beta^2\cos^2 x + \pi^2 k^2}\cos(nx)dx \quad (8)$$

It can be immediately observed that all a_{nk} with even $n \geq 2$ are equal to zero. Using Equations 6 and 7 and inverting the order of the summations, one gets:

$$L(x) = \sum_{k=1}^{\infty} a_{0k} + 2\sum_{n=1}^{\infty}\left(\sum_{k=1}^{\infty} a_{nk}\right)\cos(nx) \quad (9)$$

where the outer sum of the second term is intended over odd integers only. The amplitudes A_n of the various terms $\cos(nx)$ with odd n are therefore:

$$A_n = 2\sum_{k=1}^{\infty} a_{nk} \quad (10)$$

The explicit calculation of the a_{nk} coefficients is re-

ported in Appendix A. The harmonics of magnetization are given by $M_n = M_s A_n$. The harmonics of the induced voltage are $V_n \propto -nA_n$. The unknown proportionality constant between V_n and $(-nA_n)$ disappears when the results are reported in the form of a ratio between harmonics, such as $|V_n/V_1|$.

B. Properties of the solutions

The harmonics of the time-dependent Langevin function turn out to be positive for $n = 1, 5, 9...$ and negative for $n = 3, 7, 11...$ This is equivalent to say that the harmonics are either in phase with the driving field or out of phase by one half a cycle with the field (phase opposition). It is worth mentioning that such a simple phase relationship is no longer valid when magnetic hysteresis is present; in that case, all higher-order harmonics of the magnetization are out of phase by different angles with respect to the driving field [52]. In the following Sections, the absolute values of the harmonics will be mostly dealt with.

1. *Behaviour of $|A_n|$ with the order of harmonic*

The ratio of $|A_n/A_1|$ (up to $n = 17$) is plotted as a function of n in the left panel of Figure 1 for particle diameters ranging from 9 to 29 nm, $H_V = 100$ Oe, $T = 300$ K and $M_s = 300$ emu/cm^3, typical of magnetite particles used in high-frequency applications. For small diameters, the amplitude of the harmonics dramatically drops with increasing n; the slope becomes increasingly less steep with increasing D. The effect of particle polydispersity is shown in the same panel using a lognormal distribution of particle sizes with mode $D_m = 16$ nm and standard deviation $\sigma = 0.2$. A distribution of particle sizes introduces a marked upward curvature in this representation of the $|A_n/A_1|$ vs. n behaviour.
The corresponding behaviour of the harmonics of the induced voltage is shown for comparison in the right panel, in the form $|V_n/V_1|$. The curvature predicted for the harmonics of both $M(t)$ and $V(t)$ is in qualitative agreement with the upward curvature of the amplitudes of harmonics often measured by MPS on actual systems of immobilized nanoparticles, where the presence of a wide dispersion of effective particle sizes is well known [36, 53, 54].

2. *Behaviour of A_n with the parameter β*

The behaviour of the absolute value of A_n with the parameter $\beta = M_s V H_V / k_B T$ is shown in the left panel of Figure 2 for $n = 1 - 11$. All spectral harmonics start from zero at $\beta = 0$; it can be easily shown that in the limit $\beta \to 0$ the n-th harmonic goes as β^n; for instance, $A_1 \approx (1/6)\beta$, $A_3 \approx -(1/360)\beta^3$, $A_5 \approx (1/15120)\beta^5$, and so on. The harmonics monotonically increase with increasing β, reflecting the increasing effect of the non-linearity of the Langevin function, and finally reach asymptotic values for $\beta \to \infty$. It can be shown that the asymptotic value is $|A_n|_\infty = 4/n\pi$ for any n. The explicit calculation for $n = 1$ is done in the Supplemental Material 1. As a direct consequence, the absolute values of all harmonics of the induced voltage tend to the same asymptotic value in the limit $\beta \to \infty$. Therefore, the higher-order harmonics of the induced voltage grow more rapidly than the ones of magnetization with increasing β, as shown in the right panel of Figure 2, where the quantity $|nA_n|$, proportional to $|V_n|$, is reported. For instance, in large particles still described by the Langevin function the harmonics of the induced voltage tend to become level.

It is worth noting that the for sufficiently high β the amplitude of the first harmonic of the time-dependent Langevin function is larger than 1, its maximum value being $4/\pi \approx 1.2732$ for $\beta \to \infty$. Such a rather counter-intuitive result (the reduced magnetization $M(t)/M_s \equiv L(\omega t)$ cannot exceed unity) is explained considering that the total $M(t)/M_s$ waveform is the sum of an infinite number of terms of opposite sign which partially compensate each other. Its maximum value can be shown to be exactly 1, as expected; however, such a limit can be overcome by the amplitude of a single harmonic, as is actually the case for $n = 1$. In particular, A_1 becomes greater than unity for $\beta \gtrsim 6.78$. The point is discussed in more detail in the Supplemental Material 2. This fact can have some practical consequences: the picked-up signal which can be obtained, e,.g., by filtering and keeping a number of harmonics having the same sign (such as the ones with $n = 1$, 5, 9,...) can be significantly larger and therefore more treatable than the overall signal obtained when all harmonics are present. In actual applications of MPS this effect can help increase the sensitivity of the method.

3. *Probing superparamagnetism at high frequency*

In dc magnetization measurements, a way to check whether nanoparticles are in the superparamagnetic regime is to plot the reduced magnetization $M(H)/M_s$ as a function of the ratio H/T, because all curves measured on a bona fide superparamagnetic system at different temperatures and/or at different fields become perfectly superimposed [33].
A closely similar behaviour can be observed in high-frequency measurements, provided that the role of the dc magnetic field is taken now by the vertex field H_V. This is shown in Figure 3, where the values of A_1 and $|A_3|$ calculated for 15 nm particles at various values of H_V and at four different temperatures are shown to perfectly superimpose when the independent variable is taken as H_V/T. Such a procedure could be useful to experimen-

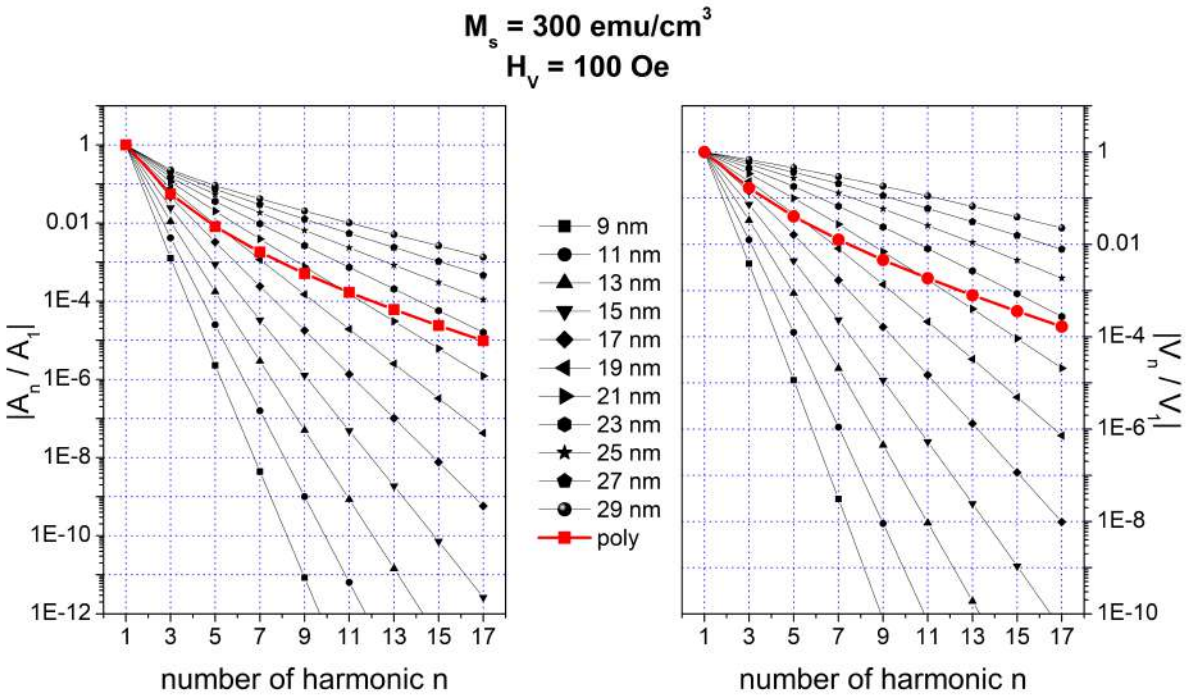

FIG. 1. Left panel: black symbols: room-temperature behaviour of the spectral harmonics of magnetization expressed as the ratio $|A_n/A_1|$ ($n \leq 17$) for various particle diameters; red symbols: polydisperse particles, with sizes distributed according to a lognormal with $D_m = 16$ nm and $\sigma = 0.2$. Right panel: the same for the ratio of the induced voltage $|V_n/V_1|$.

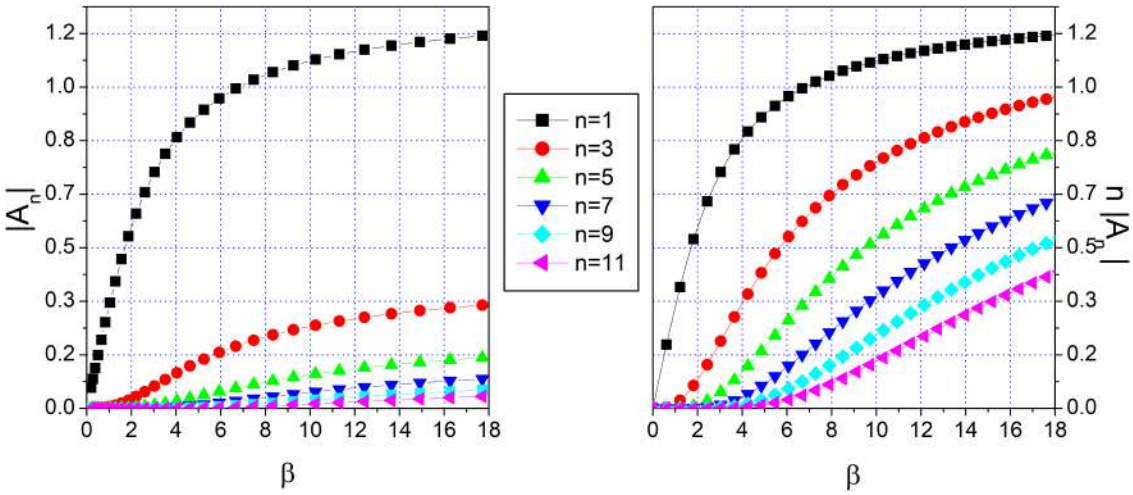

FIG. 2. Left panel: behaviour with $\beta = M_s V H_V / k_B T$ of the absolute value of the amplitude of the first six spectral harmonics of the time-dependent Langevin function; right panel: the same for the quantity nA_n (proportional to the n-th harmonic of the induced voltage V_n)

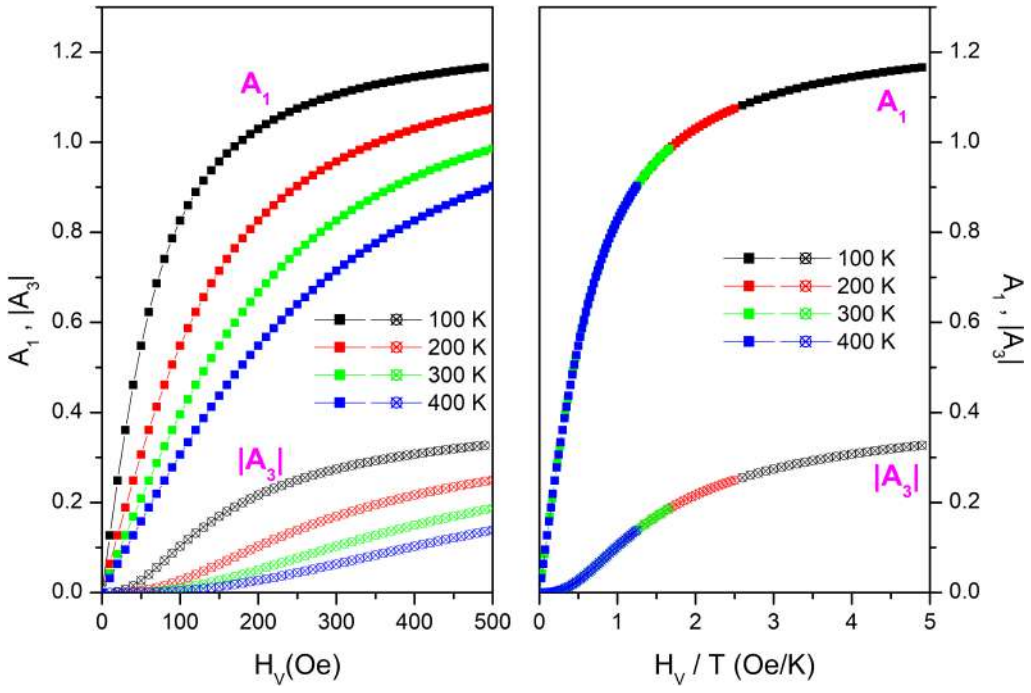

FIG. 3. Left panel: behaviour of A_1 and $|A_3|$ with the vertex field H_V at four different temperatures for particles with $D = 15$ nm and $H_s = 300$ emu/cm^3; right panel: the single curve resulting for both harmonics when these are plotted as functions of H_V/T.

tally check whether immobilized particles, measured to be superparamagnetic in quasi-static conditions, can still be taken as superparamagnetic at the typical operating frequencies of MPS or MPI.

IV. REAL NANOPARTICLES: AN EXPERIMENTAL CHECK

Superparamagnetic nanoparticles commonly used in present-day high-frequency applications such as MPS and MPI are either produced or characterized as magnetic suspensions in a fluid. When submitted to a high-frequency driving field, their magnetic response is in general determined by a combination of effects arising from Brown's and Néel's relaxation mechanisms [17, 20]. The theory developed in the previous Section applies to the latter case only, under the additional restrictive hypothesis that Néel's relaxation time is short compared to one period of the driving field. This case is however of particular interest in MPS and in precision medicine diagnostics where the nanoparticles are immobilized within a living tissue [55, 56]. In any case, MPS is a rather versatile technique of characterization not limited to the study of magnetic suspensions and can be applied to samples made of immobilized particles as well.

A second important aspect is the actual nature of the magnetic response of nanoparticles at high frequency (typically between 10 and 30 KHz in most applications). In fact, nanoparticles observed to be superparamagnetic in dc measurements may display hysteretic properties when magnetized at high frequency, as theoretically predicted [52, 57] and experimentally verified [58]. In that case, the particle's magnetization is no longer in thermal equilibrium during one driving field's period [38] and the time-dependent Langevin function fails to give an accurate picture of the magnetic response.

Several experimental MPS spectra of immobilized particles have been published in the last decade [36, 58–63]; the results can be analyzed to check whether the magnetic response of nanoparticles can still be described in terms of the Langevin function or not. In the following Sections, experimental results on immobilized nanoparticles of magnetite (Fe_3O_4) will be discussed in some detail. The nanoparticles were prepared with different techniques and submitted to MPS analysis using different driving frequencies and vertex field amplitudes.

A. Behaviour of the amplitude with the order of the harmonics

The experimental magnetization spectrum of magnetite nanoparticles taken from Ref.[58] is shown in panel (a) of Figure 4 as the ratio $|M_n/M_1| \equiv |A_n/A_1|$ (red full circles). The nanoparticles (sample CMEADM-004 in Ref.[58]) were immobilized in agar and fully characterized both by dc and ac magnetic measurements. According to

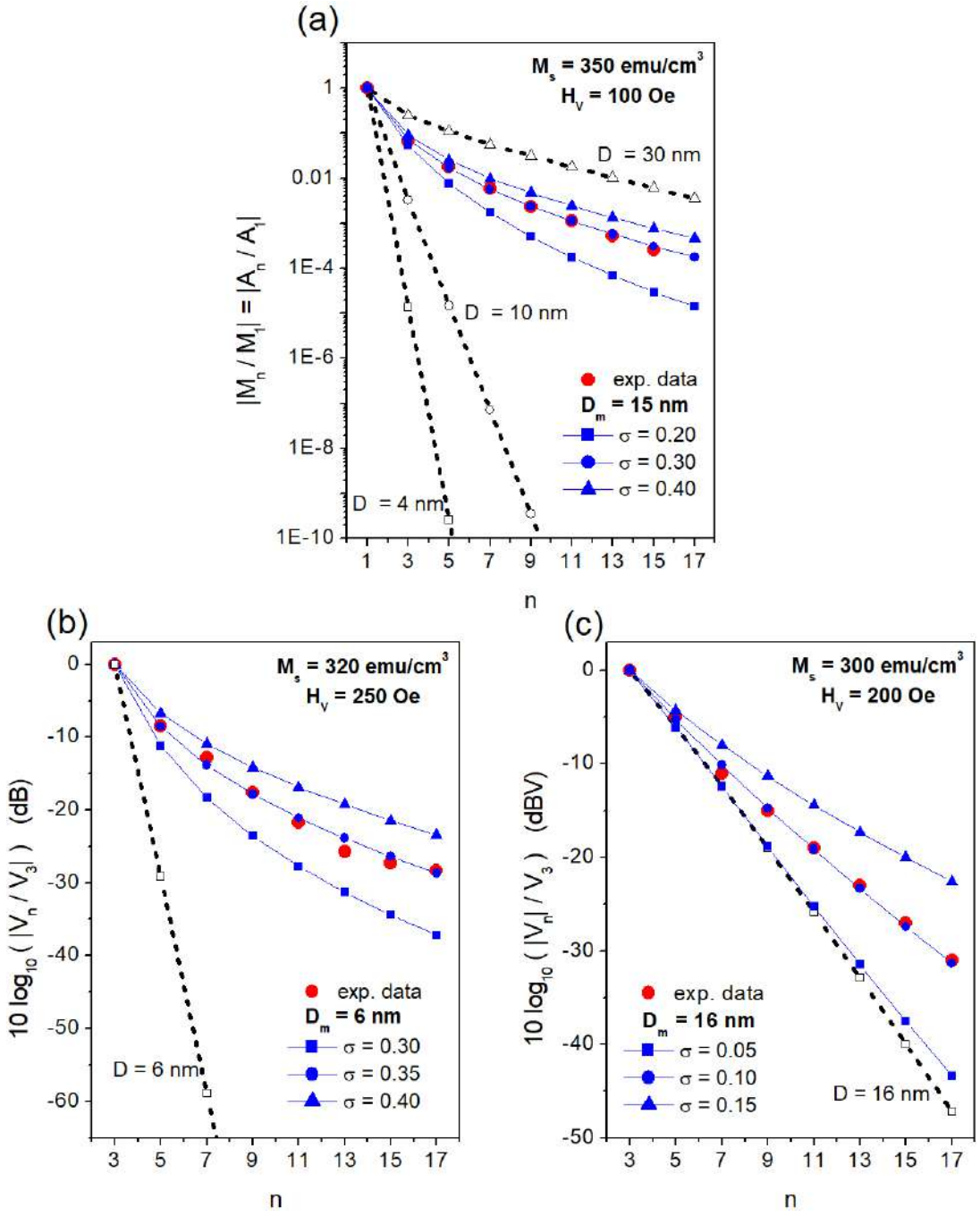

FIG. 4. Panel (a): full red circles: experimental results for $|M_n/M_1|$ measured [58] on immobilized, superparamagnetic particles of magnetite; full blue lines, with symbols: theory, for three particle size distributions of same mode and different width; black dashed lines: theory, for monodisperse particles of three different sizes. Panels (b) and (c): the same as in Panel (a) for two other experimental datasets [44, 60] obtained from samples with immobilized, superparamagnetic magnetite particles; the dashed lines shown in panels (b) and (c) apply to monodisperse particles of size corresponding to the mode of the distribution.

the Authors, the sample was made of small particles ($\approx$ 4 nm) giving rise to aggregate multi-core clusters which respond to a magnetic field as single magnetic units. The magnetic behaviour of this sample was observed to be still superparamagnetic at high frequency (10 kHz), the coercive field being negligible [58]. This sample is therefore a good candidate for an analysis done using the present theory.

The theoretically predicted behaviour of $|A_n/A_1|$ for $D = 4$ nm (corresponding to individual, single-core

nanoparticles [58]) is very far from the experimental results, a much steeper decrease of the amplitude with n being expected in this case, as shown in Figure 4 (open squares). In agreement with the general behaviour shown in the left panel of Figure 1, the experimental data suggest that the effective particle size must be considerably larger than 4 nm, confirming that multi-core aggregates exist [58]. The theoretical curves for $D = 10$ and $D = 30$ nm, reported for comparison (open circles and triangles, respectively), indicate that the size of the multi-core aggregates is in between these two sizes. In addition, the upward curvature of the experimental spectrum shows that a distribution of sizes must be present, as predicted by the theory (see Figure 1). A very good agreement between experimental data and theory is observed by assuming a lognormal distribution of effective particle sizes with mode $D_m = 15$ nm and $\sigma = 0.3$ (blue circles). The width of the distribution has a great impact on the shape of the theoretical curve, as shown by the curves drawn in panel (a) for two different values of σ (blue symbols). The present theory suggests that MPS spectra can be exploited to get information about mode and width of the distribution of effective sizes of magnetic units in a sample.

In panel (b), the theory is applied to explain the behaviour of the quantity $10\log_{10}(|V_n/V_3|)$ for the MPS spectrum of immobilized FeraSpin XS particles, as reported in Ref. [60]. In this case, the effective magnetic units were stated to be clusters of small (5-7 nm) single-core particles.[60] The agreement between theoretical prediction and measurements turns out to be very good when a lognormal distribution of mode $D_m = 6$ nm and $\sigma = 0.35$ is used. This indicates that the tendency to aggregation of single-core particles is not particularly strong in this sample, so that the effects of elementary particles are predominant. Once again, small changes of σ result in large effects on the theoretical MPS spectrum, allowing one to determine with accuracy the width of the distribution. It should be noted that the theoretical prediction for monodisperse particles with $D = 6$ nm has a much greater slope (open black symbols) and is clearly not able to fit the experimental results: this shows how much a MPS spectrum can be sensitive to the presence of a distribution of sizes. It is interesting to note that the agreement between mode and width of the size distribution determined in this work is in excellent agreement with the estimate reported by the same group in Ref. [53] on the basis of static M-H measurements.

As a further example, panel (c) shows the agreement between theory and MPS spectrum for another set of immobilized magnetite nanoparticles [44]. In this case, the experimental spectrum does not exhibit any apparent upward curvature, indicating that the distribution of effective sizes must be narrow, more in agreement with the theoretical behaviour predicted for monodisperse nanoparticles shown in Figure 1. This is confirmed by the small values of σ required to fit the experimental spectrum in the present case. The prediction for strictly monodisperse particles with $D = 16$ nm is reported for comparison (black open symbols).

The general agreement between theory and experiment indicates that even the last two samples still behave as superparamagnetic materials at the operating frequency.

B. Behaviour of harmonics with the vertex field

MPS spectra were measured at selected vertex fields at the frequency of 69 kHz on immobilized magnetite nanoparticles which had been previously characterized [64, 65]. Details about the high-frequency measurement technique are given in the Supplemental Material 3. The individual particles were shown to be described by a narrow Gaussian distribution peaked at 5.6 nm. The amplitudes of the first and third harmonic of the magnetization, $M_1 = M_s A_1$ and $M_3 = M_s|A_3|$ are reported in Figure 5 (red full circles).

The experimental behaviour of M_1 with H_V (panel (a)) is in excellent agreement, in absolute value and shape, with the theory when a lognormal distribution of effective sizes with mode $D_m = 9.6$ nm and $\sigma = 0.1$ is used (blue dashed line). On the other hand, the theoretical prediction for $D = 5.6$ nm is definitely unable to fit the experimental results (black dashed line). The fitting parameters indicate that the nanoparticles aggregate to form small clusters, in agreement with the conclusions drawn from the analysis of dc magnetic properties [65].

On the other hand, the experimental results for M_3 (panel (b)) are in good agreement with the theoretical prediction for the three lowest vertex fields only (keeping the same theoretical parameters as in the analysis of M_1). For higher vertex fields, the third harmonic keeps growing with H_V without however following the theoretical curve (blue dashed line).

The deviation of the experimental data from the theoretical prediction for the two highest vertex fields may indicate that the Langevin function is no longer able to describe the $M(H)$ curve of the sample. In fact, thermal equilibrium is more difficult to be maintained by the nanoparticles when the inversion of the magnetization in one driving field's period becomes larger, as it happens for high vertex fields. This conclusion is supported by the emergence of a magnetic hysteresis loop which appears at large vertex fields only, as shown in the Supplemental Material 4.

The present discussion suggests that the third harmonic is more sensitive than the first one to the onset of magnetic hysteresis. It should be finally noted that for strictly monodisperse particles with $D = 5.6$ nm the third harmonic would be vanishingly small, as shown in panel (b) (black dashed line).

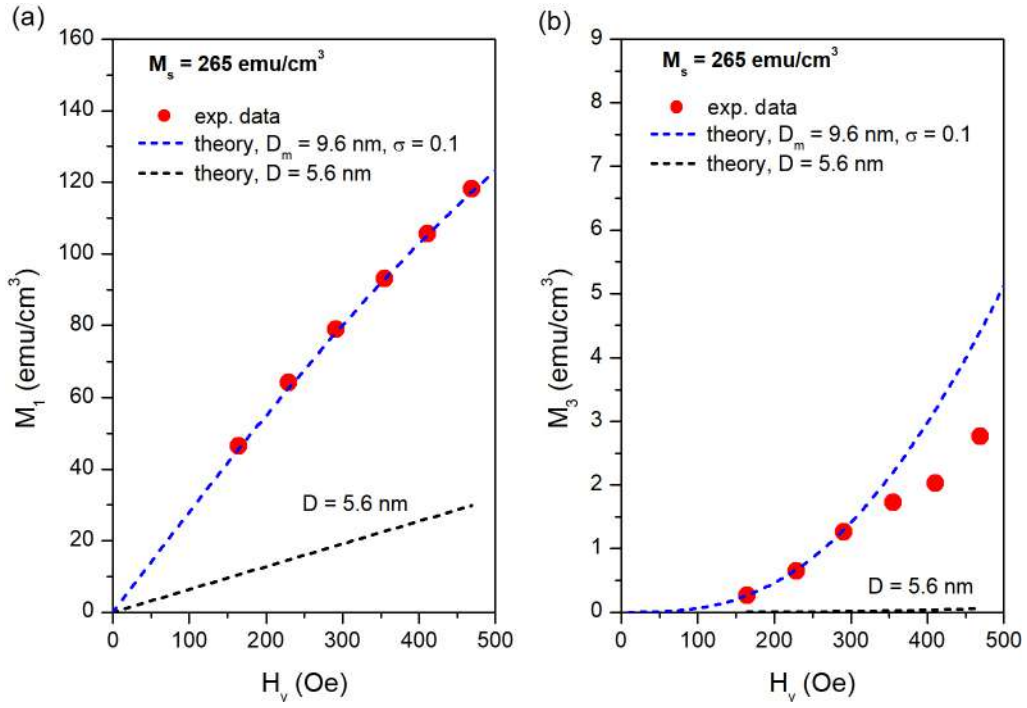

FIG. 5. Panel (a): Red full circles: first harmonic of the magnetization measured at 69 kHz on magnetite nanoparticles as a function of the vertex field; blue dashed line: theoretical prediction for a realistic distribution of nanoparticle sizes (see text); black dashed line: theoretical prediction for monodisperse nanoparticles of diameter equal to the average size determined by TEM. Panel (b): the same as in panel (a) for the third harmonic of the magnetization. The third harmonic is predicted to be very close to zero for monodisperse nanoparticles of diameter equal to the average size determined by TEM.

V. ANALYTIC EXPRESSION OF THE SYSTEM FUNCTION IN MPI

Magnetic tracers for MPI are usually considered to be superparamagnetic particles with magnetization described by the Langevin function whose intrinsic nonlinearity is the key factor to build a MPI map of the scanned tissue. Usually, a MPI device works by detecting higher-order harmonics of the induced signal: the third harmonic is often exploited in actual devices. In a standard MPI scanning procedure the vertex field H_V is constant, while different points of the scanned tissue correspond to different values of the bias field H_0, as determined by a static magnetic-field gradient [25, 34]. The $|A_3(H_0)|$ curve is called system function [47].

When $H_0 \neq 0$, the third harmonic of the magnetization cannot be obtained from Equation 4. However, the desired result can be achieved by separately using Equations 3 and 5 in their own regions of validity, corresponding to the conditions $H_0 < [(6k_BT/M_sD^3) - H_V]$ and $H_0 \geq H_V$, respectively. The bias field H_0 can be shown to satisfy to both inequalities if $D < (3k_BT/M_sH_V)^{1/3}$. Such a condition is fulfilled by particles still superparamagnetic at the operating frequencies for the typical values of H_V used in the MPI practice. As an example, using $M_s = 300$ emu/cm^3, $H_V = 100$ Oe, the maximum particle size guaranteeing that the two solutions overlap is about 16 nm.

A. Solution for small H_0

When $H_0 < [(6k_BT/M_sD^3) - H_V]$, the exact solution for the amplitude of the third harmonic of the magnetization $M_3 = M_sA_3$ with H_0 turns out to be:

$$M_3(H_0) = M_s \sum_{k=2}^{\infty} \frac{2^{2k}}{(2k)!} B_{2k}\, \gamma^{2k-1}\, C_{2k-1}(H_0) \qquad (11)$$

where $\gamma = M_sV/k_BT$, B_{2k} is the $(2k)$-th Bernouilli number, and the function $C_{2k-1}(H_0)$ is defined as:

$$C_{2k-1}(H_0) = \\ = \sum_{h=1}^{k-1} \frac{(2k-1)!}{(2k-2h-2)!(h-1)!(h+2)!}\, H_V^{2h+1}\, H_0^{2k-2h-2} \qquad (12)$$

for $k \geq 2$. The explicit calculation leading from Equation 3 to Equations 11-12 can be found in Appendix B.

B. Solution for large H_0

When $H_0 \geq H_V$, the exact solution for the amplitude of the third harmonic of the magnetization M_3 with H_0 turns out to be:

$$M_3(H_0) = M_s \sum_{k=2}^{\infty} \left[\frac{1}{2^{2k-2}} \frac{(2k-1)!}{(k-2)!(k+1)!} \times \right. \\ \left. \times \left(\frac{H_V^{2k-1}}{\gamma H_0^{2k}} - \frac{2\sigma^{2k-1}}{(2k-1)!} P_k(H_0) \right) \right] \quad (13)$$

where $\gamma = M_s V/k_B T$, $\sigma = 2\gamma H_V$ and the functions $P_k(H_0)$ are defined as:

$$P_k(H_0) = \sum_{n=1}^{\infty} n^{2k-1} e^{-2n\gamma H_0} \quad (14)$$

k being any positive integer starting from $k = 2$. The explicit calculation leading from Equation 5 to Equations 13-14 is reported in Appendix C.

C. Overall behaviour of $|M_3(H_0)|$

The behaviour of the system function $|M_3(H_0)|$ with $H_V = 100$ Oe is reported in Figure 6, panels (a-b), in the interval $0 \leq H_0 \leq 1$ kOe for six particle diameters (with $M_s = 300$ Oe) at room temperature. In the studied cases, the two solutions overlap over an extended range of H_0 values, so that a single continuous curve can be drawn. The ranges of validity of the two partial solutions are shown in the Supplemental Material 5.

It should be noted that for $H_0 = 0$ as well as for small bias fields, the actual amplitude of the third harmonic is negative: this means that this harmonic of the time-dependent Langevin function and the driving field are initially in phase opposition. Although the details of the solutions are strongly depending on particle size, a number of common features of these curves can be put in evidence. The absolute maximum of the $|M_3(H_0)|$ function is always in the origin ($H_0 = 0$). With increasing H_0, the absolute value of M_3 decreases and becomes zero at a field $H_0 = H_0^{[Z]}$ which strongly depends on nanoparticle size. Above $H_0^{[Z]}$ the solution for M_3 becomes positive; in other words, at $H_0 = H_0^{[Z]}$ a sudden change of the phase of the third harmonic with respect to the driving field takes place (from π to 0). Above $H_0^{[Z]}$ the $|M_3|$ function rises again to a single secondary maximum and finally goes to zero for $H_0 \to \infty$.
The effect of a distribution of particle sizes is dealt with in the Supplemental Material 6.

D. Estimating the positions of the zero and of the secondary maximum of the system function

In terms of the SF, as defined in the usual MPI procedure, the closer $H_0^{[Z]}$ is to zero, the higher the resolution of the technique. On the other hand, the presence of the secondary maximum should be taken in due consideration in the treatment of the picked-up signal. The analytic solution allows one to easily predict where the SF is zero and where it reaches the secondary maximum: Equation 13 can be exploited to accurately estimate the positions of both quantities.

Putting equal to zero the first term of the development of Equation 13 ($k = 2$), one gets:

$$M_3(H_0) \approx M_s \left(\frac{H_V^3}{\gamma H_0^4} - \frac{2\sigma^3}{3!} P_2(H_0) \right) = 0 \quad (15)$$

where $P_2 = \sum_{n=1}^{\infty} n^3 e^{-2n\gamma H_0}$. Using the definition of σ, Equation 15 can be written as:

$$\sum_{n=1}^{\infty} n^3 e^{-2n\gamma H_0^{[Z]}} - \frac{3}{8} \frac{1}{\left(\gamma H_0^{[Z]}\right)^4} = 0 \quad (16)$$

The left side term can be easily summed up:

$$\sum_{n=1}^{\infty} n^3 e^{-2n\gamma H_0^{[Z]}} = \frac{e^{6\gamma H_0^{[Z]}} + 4e^{4\gamma H_0^{[Z]}} + e^{2\gamma H_0^{[Z]}}}{\left(e^{2\gamma H_0^{[Z]}} - 1\right)^4} \quad (17)$$

so that the approximate value of $H_0^{[Z]}$, i.e., the position of the zero of $|A_3|$ on the H_0 axis, is immediately obtained by solving the equation:

$$\frac{e^{6\gamma H_0^{[Z]}} + 4e^{4\gamma H_0^{[Z]}} + e^{2\gamma H_0^{[Z]}}}{\left(e^{2\gamma H_0^{[Z]}} - 1\right)^4} - \frac{3}{8} \frac{1}{\left(\gamma H_0^{[Z]}\right)^4} = 0 \quad (18)$$

The agreement between approximate and exact values of the position of the zero for different particle sizes is very good, as shown in panel (c) of Figure 6. As expected, the larger the particle size is, the lower $H_0^{[Z]}$.

A closely similar procedure can be exploited to derive the position of the secondary maximum, $H_0^{[SM]}$, which is obtained putting equal to zero the first derivative of M_3. Considering the term with $k = 2$ only, one gets:

$$\frac{dM_3}{dH_0} \approx M_s \left(-\frac{4H_V^3}{\gamma H_0^5} - \frac{2\sigma^3}{3!} \frac{dP_2}{dH_0} \right) = 0. \quad (19)$$

Using $dP_2/dH_0 = -2\gamma \sum_{n=1}^{\infty} n^4 e^{-2n\gamma H_0}$, one gets:

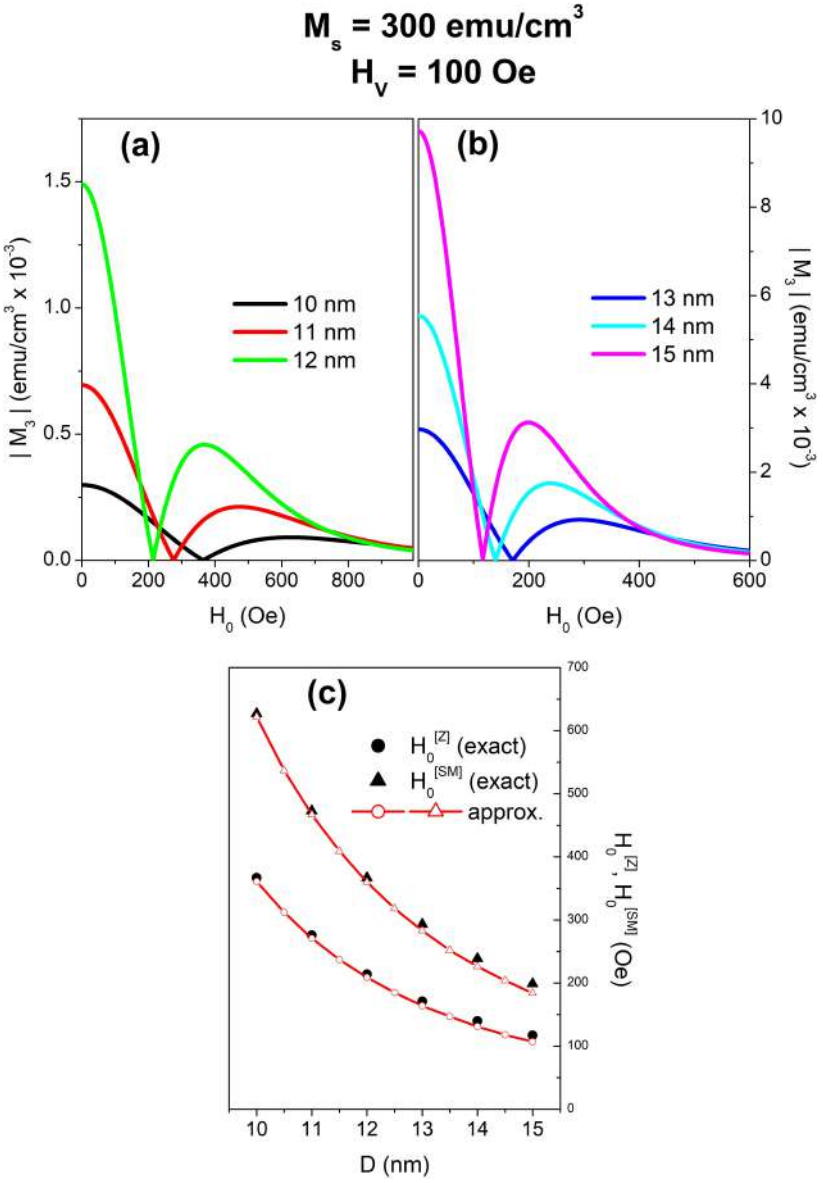

FIG. 6. Panels (a-b): behaviour of the system function $|M_3(H_0)|$ for particle diameters in the range 10-15 nm with M_s = 300 emu/cm^3, submitted to a driving field of amplitude H_V = 100 Oe; panel (c): comparison between exact and approximate values of the position of the zero and of the secondary maximum of the SF for particle diameters in the interval 10-15 nm.

$$\sum_{n=1}^{\infty} n^4 e^{-2n\gamma H_0^{[SM]}} - \frac{3}{4}\frac{1}{\left(\gamma H_0^{[SM]}\right)^5} = 0 \qquad (20)$$

Solving this implicit equation gives the approximate value of $H_0^{[SM]}$, i.e., the position of the secondary maximum of M_3 on the H_0 axis. Even in this case the agreement between approximate and exact values of the position of the secondary maximum for different particle sizes is very good, as shown in panel (c) of Figure 6. Once again, the larger the particle size is, the lower $H_0^{[SM]}$.

E. Effect of vertex field on the system function

The theory shows that the SF is a function not only of the bias field by also of the amplitude of the driving field H_V, a fact not always acknowledged in the literature. One expects that the magnitude of the third harmonic (as well as of all higher-order spectral harmonics of $M(t)$) should be enhanced with increasing H_V as the nonlinear features of the Langevin function become more and more important. Transforming Equation 11, the behaviour of $M_3(H_V)$ for $H_0 = 0$ can be easily expressed as:

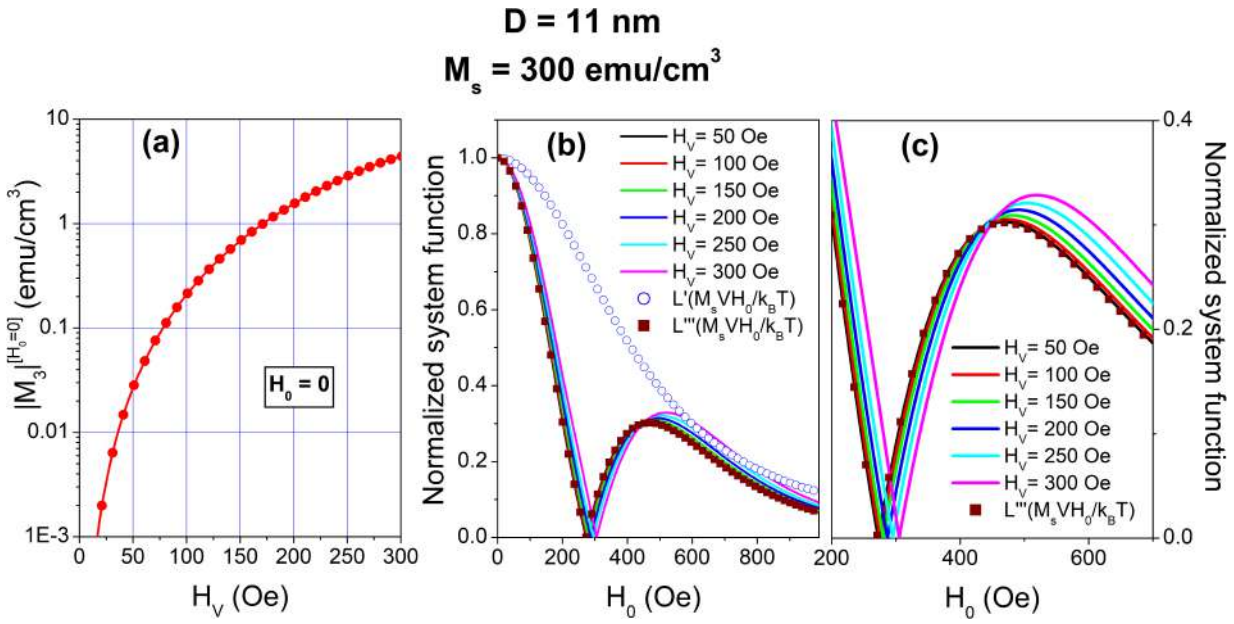

FIG. 7. Effect of vertex field on the SF of monodisperse particles ($D = 11$ nm, $M_s = 300$ emu/cm^3). Panel (a): behaviour of $|M_3^{[H_0=0]}|$ as a function of H_V (note the logarithmic vertical scale); panel (b): SFs normalized to the maximum value for some values of H_V (lines); first derivative of the Langevin function (open circles); third derivative of the Langevin function (full squares); panel (c) region around the zero and the secondary maximum of the SF.

$$M_3^{[H_0=0]}(H_V) = \\ = 4M_s \sum_{k=2}^{\infty} \frac{1}{2k} B_{2k} \frac{1}{(k-2)!(k+1)!} \gamma^{2k-1} H_V^{2k-1} \approx \\ \approx M_s \Big[-\frac{1}{180}(\gamma H_V)^3 + \frac{1}{1512}(\gamma H_V)^5 - ... \Big] \quad (21)$$

The absolute value of $M_3^{[H_0=0]}$ is reported as a function of H_V in panel (a) of Figure 7 for particles with $D = 11$ nm and $M_s = 300$ emu/cm^3 (note the logarithmic vertical scale). The effect of H_V on the maximum value of the SF (and in general on the whole SF) is remarkable: changing H_V by a factor 4 (e.g., from 50 to 200 Oe) results in an enhancement of the signal of a factor of about 50.

H_V affects the shape of the SF also, as shown in panels (b-c) of Figure 7 where some SFs obtained using different H_V and normalized to their maximum values are plotted as functions of H_0. In the panels, the third derivative of the Langevin function of argument (γH_0) normalized to its maximum value is also reported (full squares). As a matter of fact, it can be analytically proven that in the limit $H_V \to 0$, $M_3(H_0)$ becomes proportional to the third derivative of the Langevin function; note however that the maximum amplitude of $M_3(H_0)$ becomes vanishingly small in this limit.

For larger values of H_V the $M_3(H_0)$ function is no longer proportional to the third derivative of the Langevin function, the deviation becoming increasingly larger with increasing H_V. Increasing the vertex-field amplitude brings about a very limited loss of resolution of the SF largely counterbalanced by a strong enhancement of the signal.

The curve drawn using open circles in panel (b) represents the behaviour of the first derivative of the Langevin function of argument (γH_0) normalized to its maximum value. In some cases, such a derivative is used for a first-hand determination of the achievable spatial resolution and sensitivity of the method [27, 66–68]. Panel (b) of Figure 7 shows that this is just a good monotonic representation of a more structured curve.

VI. CONCLUSIONS

In this paper, a complete analytical theory of the time-dependent Langevin function has been developed. The theory can be applied to immobilized superparamagnetic nanoparticles whose magnetization by effect of a harmonic driving field is still close to equilibrium even at the operating frequencies typical of applications such as MPS and MPI (tens of kHz).

The rich frequency spectrum of the dynamical magnetization of nanoparticles is determined starting from suitable developments of the Langevin function. The main results of the theory are:

- the amplitudes of the spectral harmonics of magnetization and induced voltage are exactly known for any

value of the driving field amplitude H_V;
- an upper limit of the amplitudes of the spectral harmonics is predicted;
- the amplitude of the first harmonic of the magnetization can become larger than the amplitude of the whole magnetization;
- a MPS signal can be enhanced by spectral harmonics filtering, increasing the sensitivity of the technique;
- a method to verify the high-frequency superparamagnetic behaviour of nanoparticles is proposed ;
- an analytic expression for the system function of MPI is given;
- the role of particle size and driving field's amplitude on the system function is clarified;
- simple expressions for the positions of the zero and the secondary maximum of the system function are obtained.

The theory has been successfully compared to experimental results on immobilized magnetite nanoparticles. The excellent agreement between theory and experiment indicates that the examined samples were indeed made of superparamagnetic particles.

Deviations of experimental results from the exact theoretical prediction can be now definitely ascribed to the fact that the magnetization of nanoparticles does not follow the Langevin function, ruling out uncertainties arising from the use of an approximate theory. This outcome is important in some practical applications, because the disagreement between measured and theoretical spectral harmonics implies that at the operating frequency magnetic hysteresis is no longer negligible. The latter circumstance can result in undesired or even harmful effects (such as heating of tissues) in specific diagnostic applications.

Finally, an exact theory turns out to be helpful both in testing more advanced numerical simulations of the high-frequency behaviour of magnetic nanoparticles and in calibrating a measurement setup. In the first case, the adequacy of any numerical simulation of realistic nanoparticle systems including more complex effects, such as e.g. interparticle interactions, can be previously assessed by verifying the model's ability to correctly simulate the behaviour of virtual superparamagnetic, non-interacting particles - which has to be coincident with the one predicted by the present theory. In the second case, measurements done on a reference sample containing particles of known physical properties and morphology, still superparamagnetic at the operating frequency, may be used to correctly calibrate a measurement setup with the aid of the quantitative predictions of the theory.

Appendix A: MPS: harmonics of $M(t)$

The a_{nk} coefficients (for odd n) of the Fourier series of Equations 7-10 are obtained by solving integrals of the type:

$$a_{nk} = \frac{1}{\pi}\int_{-\pi}^{\pi} \frac{\beta\cos x}{\beta^2\cos^2 x + k^2\pi^2}\,\cos(nx)dx$$

Each $\cos(nx)$ term with odd n can be represented in terms of odd powers of $\cos x$ according to the rule [51]:

$$\begin{aligned}\cos(nx) = 2^{n-1}\cos^n x - \frac{n}{1}\binom{n-1}{0}2^{n-3}\cos^{n-2} + \\ + \frac{n}{2}\binom{n-3}{1}2^{n-5}\cos^{n-4} - \frac{n}{3}\binom{n-4}{2} + \\ + 2^{n-7}\cos^{n-6} + ... \pm n\cos x\end{aligned}$$

where $\binom{a}{b} = a!/[b!(a-b)!]$ and the sign of the last term is positive when $n = 5, 9, 13, ...$ and negative when $n = 3, 7, 11, ...$

Therefore, each a_{nk} term can be written as a finite sum of integrals:

$$\begin{aligned}a_{nk} = 2^{n-1}I_{n+1} - \\ - \frac{n}{1}\binom{n-1}{0}2^{n-3}I_{n-1} + \frac{n}{2}\binom{n-3}{1}2^{n-5}I_{n-3} - \\ - \frac{n}{3}\binom{n-4}{2}2^{n-7}I_{n-5} + ... \pm nI_2\end{aligned} \tag{A.1}$$

with

$$I_m = \frac{1}{\pi}\int_{-\pi}^{\pi}\frac{\beta\cos^m x}{\beta^2\cos^2 x + k^2\pi^2}dx$$

where m is always an even number taking the values 2, 4, 6, ... Three a_{nk} terms are explicitly given below:

$$\begin{gathered}a_{1k} = I_2 \\ a_{3k} = 4\ I_4 - 3I_2 \\ ..... \\ a_{9k} = 256\ I_{10} - 576\ I_8 + 432\ I_6 - 120\ I_4 + 9\ I_2 \\ .....\end{gathered}$$

The integrals I_m can be obtained by recursion starting from I_2, which is easily calculated:

$$\begin{aligned}I_2 = &\frac{1}{\pi}\int_{-\pi}^{\pi}\frac{\beta\cos^2 x}{\beta^2\cos^2 x + k^2\pi^2}dx = \\ &= \frac{2}{\beta}\left[1 - \frac{1}{\left(1+\frac{\beta^2}{k^2\pi^2}\right)^{1/2}}\right]\end{aligned} \tag{A.2}$$

It can be checked that:

$$I_4 = \frac{1}{\beta} - \frac{k^2\pi^2}{\beta^2}I_2$$

$$I_6 = \frac{3}{4}\frac{1}{\beta} - \frac{k^2\pi^2}{\beta^2} I_4$$

and, in general, for any even $m > 2$:

$$I_m = \frac{1}{2^{m-3}} \binom{m-2}{\frac{m}{2}-1} \frac{1}{\beta} - \frac{k^2\pi^2}{\beta^2} I_{m-2}$$

As a consequence, all a_{nk} terms with arbitrary odd n can be obtained from Equation (A.1). The results are to be inserted in Equation 10 of the main text.

Appendix B: Calculation of $A_3(H_0)$ for small H_0

When the argument y of Equation 3 is $y = \gamma[H_0 + H_V \cos(\omega t)]$ where $\gamma = (M_s V/k_B T)$, the expression of the time-dependent Langevin function for sufficiently small H_0 becomes:

$$L(\omega t) = \sum_{k=1}^{\infty} \frac{2^{2k}}{(2k)!} B_{2k}\, \gamma^{2k-1} [H_0 + H_V \cos(\omega t)]^{2k-1} \tag{B.1}$$

This series contains all powers of $\cos(\omega t)$ and should be transformed into a Fourier series of cosines.

Here, we are interested in the amplitude of the term in $\cos(3\,\omega t)$ only. Each binomial term of the power series, $[H_0 + H_V \cos(\omega t)]^{2k-1}$, can be expanded as a finite sum of powers of $\cos(\omega t)$. Such a sum contains all even and odd powers of $\cos(\omega t)$ from 0 to $(2k-1)$. By making use of the representation of powers of the cosine function in terms of the cosines of multiples of the argument [51], it can be easily checked that the amplitude of the third harmonic of the Fourier series is determined by all odd powers larger than 1 in the expansion of the binomial: on the contrary, all even powers of the cosine and the linear term in $\cos(\omega t)$ do not contribute to the amplitude of the third harmonic.

By properly taking into account *(a)* the coefficients of the standard binomial expansion and *(b)* the coefficients associated to the the term in $\cos(3\,\omega t)$ when each odd power of $\cos(\omega t)$ is transformed into the cosines of multiples of the argument, it is possible to get a general expression for the total contribution to the third harmonic of the generic $(2k-1)$-th term of the series of Equation B.1.

As an example of the procedure, let us consider the term $[H_0 + H_V \cos(\omega t)]^5$, whose expansion reduces to: $[10 H_0^2 H_V^3 \cos^3(\omega t) + H_V^5 \cos^5(\omega t)]$ when only the terms of the binomial development which give a contribution to $\cos(3\,\omega t)$ are kept. Now, the terms $\cos^3(\omega t)$ and $\cos^5(\omega t)$ contribute by the factors $\frac{1}{4}$ and $\frac{5}{16}$ respectively to the term $\cos(3\,\omega t)$ when the two powers of $\cos(\omega t)$ are developed in terms of the cosines of multiple angles. Therefore, the overall contribution of the 5th power of the binomial is $C_5 = \frac{10}{4} H_0^2 H_V^3 + \frac{5}{16} H_V^5 = \frac{5}{2} H_0^2 H_V^3 + \frac{5}{16} H_V^5$.

The general expression of the coefficients can be obtained by induction; as it turns out:

$$C_{2k-1} = \\ = \sum_{h=1}^{k-1} \frac{1}{2^{2h}} \frac{(2k-1)!}{(2k-2h-2)!(h-1)!(h+2)!} H_V^{2h+1} H_0^{2k-2h-2}$$

where k takes any positive integer value starting from $k = 2$. This expression allows one to easily calculate all the C_{2k-1} coefficients. The first three terms (with $k =$ 2, 3, 4) are explicitly reported here as examples of the procedure:

$$C_3 = \frac{1}{4} \frac{(3)!}{(0)!(0)!(3)!} H_V^3 H_0^0 = \frac{1}{4} H_V^3$$

$$C_5 = \frac{1}{4} \frac{(5)!}{(2)!(0)!(3)!} H_V^3 H_0^2 + \frac{1}{16} \frac{(5)!}{(0)!(1)!(4)!} H_V^5 H_0^0 = \\ = \frac{5}{2} H_V^3 H_0^2 + \frac{5}{16} H_V^5$$

$$C_7 = \frac{1}{4} \frac{(7)!}{(4)!(0)!(3)!} H_V^3 H_0^4 + \frac{1}{16} \frac{(7)!}{(2)!(1)!(3)!} H_V^5 H_0^2 + \\ + \frac{1}{64} \frac{(7)!}{(0)!(2)!(5)!} H_V^7 H_0^0 = \frac{35}{4} H_V^3 H_0^4 + \\ + \frac{105}{16} H_V^5 H_0^2 + \frac{21}{64} H_V^7.$$

The explicit calculation for any k is straightforward and easily implemented. Finally, all the C_{2k-1} terms must be summed up after being multiplied by the coefficients appearing in Equation B.1:

$$A_3(H_0) = \sum_{k=2}^{\infty} \frac{2^{2k}}{(2k)!} B_{2k}\, \gamma^{2k-1} C_{2k-1}(H_0).$$

This expression, multiplied by M_s, exactly corresponds to Equation 10. Note that the series begins with $k =$ 2 and contains *all* contributions to the amplitude of the third harmonic of the time-dependent Langevin function.

Appendix C: Calculation of $A_3(H_0)$ for large H_0

When the argument y of Equation 3 is $y = \gamma[H_0 + H_V \cos(\omega t)]$, the expression of the time-dependent Langevin function for $H_0 \geq H_V$ is:

$$L(\omega t) = 1 - \frac{1}{\gamma[H_0 + H_V \cos(\omega t)]} + \\ + 2\sum_{n=1}^{\infty} e^{-2n\gamma[H_0 + H_V \cos(\omega t)]} \tag{C.1}$$

The two time-dependent terms of Equation C.1 will be separately treated.

1. Transformation of the rational term

Defining $r = H_V/H_0 \leq 1$, the rational term is expanded as:

$$\frac{1}{\gamma[H_0 + H_V \cos(\omega t)]} = \frac{1}{\gamma H_0} \sum_{h=0}^{\infty} (-1)^h r^h \cos^h(\omega t) = \\ = \frac{1}{\gamma H_0} \left[1 - r\cos(\omega t) + r^2 \cos^2(\omega t) - r^3 \cos^3(\omega t) + ...\right]$$

The power series is to be transformed into a Fourier series of cosines. However, we are interested here in the third harmonic term only; following the same line of reasoning outlined in Appendix B, we look for the contributions to the third harmonic coming from all odd powers of the series development (with h larger than 1). Let us indicate each of these contributions by the symbol $\left\{\ \right\}_{[3]}$. For instance, $\left\{\cos^3(\omega t)\right\}_{[3]} = \frac{1}{4}$, $\left\{\cos^5(\omega t)\right\}_{[3]} = \frac{5}{16}$, and so on. We have therefore:

$$\left\{-\frac{1}{H_0 + H_V \cos(\omega t)}\right\}_{[3]} = \frac{1}{\gamma H_0} \sum_{k=2}^{\infty} r^{2k-1} \left\{\cos^{2k-1}(\omega t)\right\}_{[3]}$$

(note that the series contains all the odd powers of the cosine with the exclusion of the linear term). It is easy to check that each $\left\{\cos^{2k-1}\right\}_{[3]}$ term gives the following contribution to the third harmonic of the Fourier series:

$$\left\{\cos^{2k-1}(\omega t)\right\}_{[3]} = \frac{1}{2^{2k-2}} \frac{(2k-1)!}{(k-2)!(k+1)!} \tag{C.2}$$

Therefore:

$$\left\{-\frac{1}{H_0 + H_V \cos(\omega t)}\right\}_{[3]} = \\ = \frac{1}{\gamma H_0} \sum_{k=2}^{\infty} \frac{1}{2^{2k-2}} \frac{(2k-1)!}{(k-2)!(k+1)!} r^{2k-1} \tag{C.3}$$

The right-hand side of Equation C.3 gives the total contribution of the rational term to the third harmonic; it can be checked that the series converges for all $r \geq 1$.

2. Transformation of the exponential terms

Calling $\lambda_0 = e^{-2\gamma H_0}$ and $\sigma = 2\gamma H_V$, the series of exponentials in Equation C.1 can be written as:

$$\sum_{n=1}^{\infty} \lambda_0^n e^{-n\sigma\cos(\omega t)}$$

The generic exponential term of this series can in turn be developed as:

$$e^{-n\sigma\cos(\omega t)} = \sum_{h=0}^{\infty} (-1)^h \frac{\sigma^h}{h!} n^h \cos^h(\omega t) = \\ = 1 - n\sigma\cos(\omega t) + \frac{1}{2!} n^2\sigma^2 \cos^2(\omega t) - \\ - \frac{1}{3!} n^3\sigma^3 \cos^3(\omega t) + ...$$

The contributions to the third harmonic of the Fourier series come, as before, from all odd powers of $\cos(\omega t)$ with exponent h larger than 1; they are all negative. Using the same symbols as in the previous Section, one can write:

$$\left\{e^{-n\sigma\cos(\omega t)}\right\}_{[3]} = -\sum_{k=2}^{\infty} \frac{\sigma^{2k-1}}{(2k-1)!} n^{2k-1} \left\{\cos^{2k-1}(\omega t)\right\}_{[3]}$$

Taking into account Equation C.2, one gets for each n:

$$\left\{e^{-n\sigma\cos(\omega t)}\right\}_{[3]} = \\ = -\sum_{k=2}^{\infty} \frac{\sigma^{2k-1}}{(2k-1)!} n^{2k-1} \frac{1}{2^{2k-2}} \frac{(2k-1)!}{(k-2)!(k+1)!}$$

The total contribution to the third harmonic coming from the series of exponentials of Equation C.1 can therefore be written as:

$$\left\{2\sum_{n=1}^{\infty} \lambda_0^n e^{-n\sigma\cos(\omega t)}\right\}_{[3]} = \\ = -2\sum_{n=1}^{\infty} \left[\sum_{k=2}^{\infty} \frac{\sigma^{2k-1}}{(2k-1)!} \frac{1}{2^{2k-2}} \frac{(2k-1)!}{(k-2)!(k+1)!}\right] n^{2k-1} \lambda_0^n$$

Inverting the order of the two series and defining $P_k(H_0) = \sum_{n=1}^{\infty} n^{2k-1} \lambda_0^n$:

$$\left\{2\sum_{n=1}^{\infty} \lambda_0^n e^{-n\sigma\cos(\omega t)}\right\}_{[3]} = \\ = -2\sum_{k=2}^{\infty} \frac{\sigma^{2k-1}}{(2k-1)!} P_k(H_0) \ \ \frac{1}{2^{2k-2}} \frac{(2k-1)!}{(k-2)!(k+1)!}$$

Finally, the amplitude $A_3(H_0)$ is obtained by combining the last Equation with Equation C.3:

$$A_3(H_0) = \sum_{k=2}^{\infty} \left[\frac{1}{2^{2k-2}} \frac{(2k-1)!}{(k-2)!(k+1)!} \times \right.$$
$$\left. \times \left(\frac{r^{2k-1}}{\gamma H_0} - \frac{2\sigma^{2k-1}}{(2k-1)!} P_k(H_0) \right) \right]$$

which is coincident with Equation 13 after multiplication by M_s.

[1] Z. Zhao and C. Rinaldi, Magnetization Dynamics and Energy Dissipation of Interacting Magnetic Nanoparticles in Alternating Magnetic Fields with and without a Static Bias Field, Journal of Physical Chemistry C **122**, 21018 (2018).

[2] J. Fock, C. Balceris, R. Costo, L. Zeng, F. Ludwig, and M. Hansen, Field-dependent dynamic responses from dilute magnetic nanoparticle dispersions, Nanoscale **10**, 2052 (2018), cited By 22.

[3] A. Tomitaka, S. Ota, K. Nishimoto, H. Arami, Y. Takemura, and M. Nair, Dynamic magnetic characterization and magnetic particle imaging enhancement of magnetic-gold core-shell nanoparticles, Nanoscale **11**, 6489 (2019), cited By 17.

[4] P. Allia, G. Barrera, and P. Tiberto, Nonharmonic driving fields for enhancement of nanoparticle heating efficiency in magnetic hyperthermia, Physical Review Applied **12**, 10.1103/PhysRevApplied.12.034041 (2019).

[5] C. Shasha, K. M. Krishnan, C. Shasha, and K. M. Krishnan, Nonequilibrium Dynamics of Magnetic Nanoparticles with Applications in Biomedicine, Advanced Materials **33**, 1904131 (2021).

[6] P. Thakur, S. Taneja, D. Chahar, B. Ravelo, and A. Thakur, Recent advances on synthesis, characterization and high frequency applications of Ni-Zn ferrite nanoparticles, Journal of Magnetism and Magnetic Materials **530**, 167925 (2021).

[7] N. Neugebauer, T. Hache, M. Elm, D. Hofmann, C. Heiliger, H. Schultheiss, and P. Klar, Frequency- and magnetic-field-dependent properties of ordered magnetic nanoparticle arrangements, Physical Review B **103**, 10.1103/PhysRevB.103.094438 (2021).

[8] D. Bobo, K. J. Robinson, J. Islam, K. J. Thurecht, and S. R. Corrie, Nanoparticle-Based Medicines: A Review of FDA-Approved Materials and Clinical Trials to Date, Pharmaceutical Research **33**, 2373 (2016).

[9] C. Lu, L. Han, J. Wang, J. Wan, G. Song, and J. Rao, Engineering of magnetic nanoparticles as magnetic particle imaging tracers, Chemical Society Reviews **50**, 8102 (2021).

[10] S. Harvell-Smith, L. Tunga, and N. Thanh, Magnetic particle imaging: Tracer development and the biomedical applications of a radiationfree, sensitive, and quantitative imaging modality, Nanoscale **14**, 3658 (2021), cited By 0.

[11] M.-K. Kim, J. Sim, J.-H. Lee, M. Kim, and S.-K. Kim, Dynamical origin of highly efficient energy dissipation in soft magnetic nanoparticles for magnetic hyperthermia applications, Physical Review Applied **9**, 10.1103/PhysRevApplied.9.054037 (2018).

[12] H. Fatima, T. Charinpanitkul, and K. S. Kim, Fundamentals to Apply Magnetic Nanoparticles for Hyperthermia Therapy, Nanomaterials 2021, Vol. 11, Page 1203 **11**, 1203 (2021).

[13] K. Zhou, X. Zhou, J. Liu, and Z. Huang, Application of magnetic nanoparticles in petroleum industry: A review, Journal of Petroleum Science and Engineering **188**, 106943 (2020).

[14] K. Vamvakidis, N. Maniotis, and C. Dendrinou-Samara, Magneto-fluorescent nanocomposites: Experimental and theoretical linkage for the optimization of magnetic hyperthermia, Nanoscale **13**, 6426 (2021), cited By 0.

[15] S. Müssig, J. Reichstein, J. Prieschl, S. Wintzheimer, and K. Mandel, A Single Magnetic Particle with Nearly Unlimited Encoding Options, Small **17**, 1 (2021).

[16] A. Hakeem, T. Alshahrani, I. Ali, M. H. Alhossainy, R. Yasmin Khosa, G. Muhammad, A. R. Khan, and H. M. T. Farid, Synthesis and characterization of composites for microwave devices, Chinese Journal of Physics **70**, 232 (2021).

[17] S. Dutz, R. Hergt, and M. Zeisberger, Validity limits of the Néel relaxation model of magnetic nanoparticles for hyperthermia, Nanotechnology **21**, 5 (2010).

[18] A. Zubarev, Magnetic hyperthermia in a system of immobilized magnetically interacting particles, Physical Review E **99**, 10.1103/PhysRevE.99.062609 (2019).

[19] T. Viereck, S. Draack, M. Schilling, and F. Ludwig, Multi-spectral Magnetic Particle Spectroscopy for the investigation of particle mixtures, Journal of Magnetism and Magnetic Materials **475**, 647 (2019).

[20] K. Wu, D. Su, R. Saha, J. Liu, V. K. Chugh, and J. P. Wang, Magnetic Particle Spectroscopy: A Short Review of Applications Using Magnetic Nanoparticles, ACS Applied Nano Materials **3**, 4972 (2020).

[21] K. Wu, V. K. Chugh, V. D. Krishna, A. di Girolamo, Y. A. Wang, R. Saha, S. Liang, M. C. Cheeran, and J. P. Wang, One-Step, Wash-free, Nanoparticle Clustering-Based Magnetic Particle Spectroscopy Bioassay Method for Detection of SARS-CoV-2 Spike and Nucleocapsid Proteins in the Liquid Phase, ACS applied materials & interfaces **13**, 44136 (2021).

[22] S. Müssig, B. Kuttich, F. Fidler, D. Haddad, S. Wintzheimer, T. Kraus, and K. Mandel, Reversible magnetism switching of iron oxide nanoparticle dispersions by controlled agglomeration, Nanoscale Advances **3**, 2822 (2021), cited By 1.

[23] B. Gleich, Principles and applications of magnetic particle imaging, Principles and Applications of Magnetic

Particle Imaging , 1 (2014).
[24] S. Trisnanto and Y. Takemura, High-frequency néel relaxation response for submillimeter magnetic particle imaging under low field gradient, Physical Review Applied **14**, 10.1103/PhysRevApplied.14.064065 (2020).
[25] K. Enpuku and T. Yoshida, Magnetic particle imaging, in *Bioimaging*, edited by S. Ueno (CRC Press, Boca Raton, 2020) Chap. 7.
[26] K. Bente, A. C. Bakenecker, A. von Gladiss, F. Bachmann, A. Cebers, T. M. Buzug, and D. Faivre, Selective Actuation and Tomographic Imaging of Swarming Magnetite Nanoparticles, ACS Applied Nano Materials **4**, 6752 (2021).
[27] K. M. Parkins, K. P. Melo, Y. Chen, J. A. Ronald, and P. J. Foster, Visualizing tumour self-homing with magnetic particle imaging, Nanoscale **13**, 6016 (2021).
[28] G. Barrera, P. Allia, and P. Tiberto, Temperature-dependent heating efficiency of magnetic nanoparticles for applications in precision nanomedicine, Nanoscale **12**, 6360 (2020).
[29] D. Valdes, J. Lima, E., R. Zysler, G. Goya, and E. De Biasi, Role of anisotropy, frequency, and interactions in magnetic hyperthermia applications: Noninteracting nanoparticles and linear chain arrangements, Physical Review Applied **15**, 10.1103/PhysRevApplied.15.044005 (2021).
[30] S. Müssig, J. Reichstein, F. Miller, and K. Mandel, Colorful Luminescent Magnetic Supraparticles: Expanding the Applicability, Information Capacity, and Security of Micrometer-Scaled Identification Taggants by Dual-Spectral Encoding, Small (Weinheim an der Bergstrasse, Germany) 10.1002/SMLL.202107511 (2022).
[31] S. P. Gubin, Magnetic Nanoparticles, Magnetic Nanoparticles , 1 (2009).
[32] C. Binns, *Nanomagnetism: Fundamentals and Applications*, edited by C. Binns (Elsevier, Oxford, 2014).
[33] M. Knobel, W. C. Nunes, L. M. Socolovsky, E. De Biasi, J. M. Vargas, and J. C. Denardin, Superparamagnetism and Other Magnetic Features in Granular Materials: A Review on Ideal and Real Systems, Journal of Nanoscience and Nanotechnology **8**, 2836 (2008).
[34] A. Bakenecker, M. Ahlborg, C. Debbeler, C. Kaethner, and K. Lüdtke-Buzug, *Precision Medicine: Tools and Quantitative Approaches* (Elsevier Inc., 2018) pp. 183–228.
[35] D. B. Reeves and J. B. Weaver, Approaches for modeling magnetic nanoparticle dynamics, Critical Reviews in Biomedical Engineering **42**, 85 (2014), arXiv:1505.02450.
[36] D. Eberbeck, C. L. Dennis, N. F. Huls, K. L. Krycka, C. Gruttner, and F. Westphal, Multicore magnetic nanoparticles for magnetic particle imaging, IEEE Transactions on Magnetics **49**, 269 (2013).
[37] S. Draack, T. Viereck, F. Nording, K. J. Janssen, M. Schilling, and F. Ludwig, Determination of dominating relaxation mechanisms from temperature-dependent Magnetic Particle Spectroscopy measurements, Journal of Magnetism and Magnetic Materials **474**, 570 (2019).
[38] G. Barrera, P. Allia, and P. Tiberto, Dipolar Interactions Among Magnetite Nanoparticles For Magnetic Hyperthermia: A Rate-Equation Approach, Nanoscale **13**, 4103–412 (2021).
[39] B. Gleich and J. Weizenecker, Tomographic imaging using the nonlinear response of magnetic particles, Nature **435**, 1214 (2005).
[40] S. Biederer, T. Knopp, T. F. Sattel, K. Lüdtke-Buzug, B. Gleich, J. Weizenecker, J. Borgert, and T. M. Buzug, Magnetization response spectroscopy of superparamagnetic nanoparticles for magnetic particle imaging, Journal of Physics D: Applied Physics **42**, 205007 (2009).
[41] T. Knopp and T. M. Buzug, *Magnetic Particle Imaging* (Springer-Verlag, Berlin Heidelberg, 2012).
[42] K. Wu, D. Su, R. Saha, D. Wong, and J. P. Wang, Magnetic particle spectroscopy-based bioassays: Methods, applications, advances, and future opportunities, Journal of Physics D: Applied Physics **15**, 173001 (2019).
[43] R. M. Ferguson, K. R. Minard, A. P. Khandhar, and K. M. Krishnan, Optimizing magnetite nanoparticles for mass sensitivity in magnetic particle imaging, Medical Physics **38**, 1619 (2011).
[44] F. Ludwig, H. Remmer, C. Kuhlmann, T. Wawrzik, H. Arami, R. M. Ferguson, and K. M. Krishnan, Self-consistent magnetic properties of magnetite tracers optimized for magnetic particle imaging measured by ac susceptometry, magnetorelaxometry and magnetic particle spectroscopy, Journal of Magnetism and Magnetic Materials **360**, 169 (2014).
[45] T. Yoshida, S. Bai, A. Hirokawa, K. Tanabe, and K. Enpuku, Effect of viscosity on harmonic signals from magnetic fluid, Journal of Magnetism and Magnetic Materials **380**, 105 (2015).
[46] K. Murase and K. Shimada, Lock-in-Amplifier Model for Analyzing the Behavior of Signal Harmonics in Magnetic Particle Imaging, Open Journal of Applied Sciences **08**, 170 (2018).
[47] K. Murase, Generation of System Function Maps in Projection-Based Magnetic Particle Imaging Using Lock-in-Amplifier Model, arXiv:1901.04475 [physics.med-ph] 10.48550/arxiv.1901.04475 (2019), arXiv:1901.04475.
[48] H. Paysen, J. Wells, O. Kosch, U. Steinhoff, L. Trahms, T. Schaeffter, and F. Wiekhorst, Towards quantitative magnetic particle imaging: A comparison with magnetic particle spectroscopy, AIP Advances **8**, 056712 (2017).
[49] M. T. Rietberg, S. Waanders, M. M. Horstman-Van de Loosdrecht, R. R. Wildeboer, B. T. Haken, and L. Alic, Modelling of dynamic behaviour in magnetic nanoparticles, Nanomaterials **11**, 3396 (2021).
[50] S. Draack, M. Schilling, and T. Viereck, Magnetic particle imaging of particle dynamics in complex matrix systems, Physical Sciences Reviews , 1 (2021).
[51] I. Gradshteyn and I. Ryzhik, *Table of Integrals, Series and Products*, 7th ed. (Academic Press, 2007).
[52] G. Barrera, P. Allia, and P. Tiberto, Magnetic Nanoparticle Imaging: Insight on the Effects of Magnetic Interactions and Hysteresis of Tracers, ACS Applied Nano Materials **5**, 2699 (2022).
[53] F. Ludwig, T. Wawrzik, T. Yoshida, N. Gehrke, A. Briel, D. Eberbeck, and M. Schilling, Optimization of magnetic nanoparticles for magnetic particle imaging, IEEE Transactions on Magnetics **48**, 3780 (2012).
[54] T. Yoshida, T. Sasayama, and K. Enpuku, Effect of Core Size Distribution of Immobilized Magnetic Nanoparticles on Harmonic Magnetization, International Journal on Magnetic Particle Imaging **3**, 1703002 (2017).
[55] R. Di Corato, A. Espinosa, L. Lartigue, M. Tharaud, S. Chat, T. Pellegrino, C. Ménager, F. Gazeau, and C. Wilhelm, Magnetic hyperthermia efficiency in the cellular environment fordifferent nanoparticle designs, Biomaterials **35**, 6400 (2014).

[56] D. Soukup, S. Moise, E. Céspedes, J. Dobson, and N. D. Telling, In situ measurement of magnetization relaxation of internalized nanoparticles in live cells, ACS Nano **9**, 231 (2015).

[57] P. Allia, G. Barrera, and P. Tiberto, Hysteresis effects in magnetic nanoparticles: A simplified rate-equation approach, Journal of Magnetism and Magnetic Materials **496**, 165927 (2020).

[58] S. Ota, R. Takeda, I. Kato, S. Nohara, and Y. Takemura, Effect of particle size and structure on harmonic intensity of blood-pooling multi-core magnetic nanoparticles for magnetic particle imaging, International Journal on Magnetic Particle Imaging **3**, 1 (2017).

[59] H. Arami, R. M. Ferguson, A. P. Khandhar, and K. M. Krishnan, Size-dependent ferrohydrodynamic relaxometry of magnetic particle imaging tracers in different environments, Medical Physics **40**, 071904 (2013).

[60] N. Gehrke, A. Briel, F. Ludwig, H. Remmer, T. Wawrzik, and S. Wellert, New Perspectives for MPI: A Toolbox for Tracer Research, in *Magnetic Particle Imaging A Novel SPIO Nanoparticle Imaging Technique*, edited by M. Buzug and J. Borget (Springer, 2012) pp. 99–103.

[61] T. Yoshida, K. Enpuku, F. Ludwig, J. Dieckhoff, T. Wawrzik, A. Lak, and M. Schilling, Characterization of Resovist® Nanoparticles for Magnetic Particle Imaging, in *Magnetic Particle Imaging:A Novel SPIO Nanoparticle Imaging Technique*, edited by T. Buzug and J. Borget (Springer, 2012) pp. 3–7.

[62] T. Sasayama, T. Yoshida, and K. Enpuku, Relationship between harmonic spectra and coercive field of immobilized magnetic nanoparticles, Japanese Journal of Applied Physics **56**, 1 (2017).

[63] O. Kosch, H. Paysen, J. Wells, F. Ptach, J. Franke, L. Wöckel, S. Dutz, and F. Wiekhorst, Evaluation of a separate-receive coil by magnetic particle imaging of a solid phantom, Journal of Magnetism and Magnetic Materials **471**, 444 (2019).

[64] T. Nardi, M. Sangermano, Y. Leterrier, P. Allia, P. Tiberto, and J. A. E. Månson, UV-cured transparent magnetic polymer nanocomposites, Polymer **54**, 4472 (2013).

[65] P. Allia, G. Barrera, P. Tiberto, T. Nardi, Y. Leterrier, and M. Sangermano, Fe3O4 nanoparticles and nanocomposites with potential application in biomedicine and in communication technologies: Nanoparticle aggregation, interaction, and effective magnetic anisotropy, Journal of Applied Physics **116**, 113903 (2014).

[66] J. Rahmer, J. Weizenecker, B. Gleich, and J. Borgert, Signal encoding in magnetic particle imaging: Properties of the system function, BMC Medical Imaging **9**, 1 (2009).

[67] P. W. Goodwill and S. M. Conolly, The X-space formulation of the magnetic particle imaging process: 1-D signal, resolution, bandwidth, SNR, SAR, and magnetostimulation, IEEE Transactions on Medical Imaging **29**, 1851 (2010).

[68] M. H. Pablico-Lansigan, S. F. Situ, and A. C. S. Samia, Magnetic particle imaging: Advancements and perspectives for real-time in vivo monitoring and image-guided therapy, Nanoscale **5**, 4040 (2013).